Light scattering from deformed droplets and droplets with inclusions. II. Theoretical treatment

Gorden Videen, Wenbo Sun, Qiang Fu, David R. Secker, Richard S. Greenaway, Paul H. Kaye, Edwin Hirst, and David Bartley

We provide theoretical results from the scattering of light by deformed liquid droplets and droplets with inclusions. With improved instrumentation and computer technologies available, researchers are able to employ two-dimensional angular optical scattering as a tool for analyzing such particle systems and which then could be applied in industrial, occupational, and military aerosol measurement. We present numerically calculated spatial light-scattering data from various droplet morphologies. We describe characteristic features of the theoretical data and compare these with the experimental results.

OCIS codes: 290.0290, 290.5850.

1. Introduction

This is the second part of a two-part paper dealing, respectively, with experimental and theoretical results from the scattering of light by deformed liquid droplets and droplets with inclusions. Deformed droplets are of importance in industrial areas involving sprays, therapeutic aerosols, and combustion aerosols, where aerodynamic particle size is commonly measured to assess the airborne behavior of the droplets. Aerodynamic particle-sizing instruments are known to produce droplet deformation during the measurement process, and this can lead to significant measurement errors.[1] Droplets with inclusions are important because they can be representative of aerosols found in hospital or battlefield environments where biological organisms can survive for prolonged periods when contained within a protective liquid coat. The *in situ* detection of these biological aerosols has attracted considerable attention recently, with laser-induced fluorescence being investigated as a way to discriminate biological from nonbiological particles.[2,3] However, because fluorescence is exhibited by many aerosol particles, discrimination based on this parameter alone has proved inefficient.

Light scattering provides an ideal means of *in situ* particle characterization or identification because it is rapid and in many cases nondestructive. Although, traditionally, light-scattering measurements were made with a single, movable detector or a limited number of fixed detectors, the advent of low-cost computer equipment and multipixel detectors such as intensified charge-coupled device cameras has made out-of-plane two-dimensional angular optical scattering (TAOS) measurements more common for the study of nonspherical or nonhomogeneous particle systems of the type mentioned above.[4–11]

At the same time that experimental apparatuses have increased in sophistication, great strides have been made on the modeling front. Although most of the credit should be given to the proliferation of fast computers, we should not overlook the modeling efforts made on irregular particles and the current algorithms developed to make the calculation of the scatter from irregular particles as simple and commonplace as the calculation of Mie scattering was a few decades ago. Modeling efforts have not only increased the efficiency of old algorithms such as the discrete dipole approximation,[12–14] the finite-difference time-domain (FDTD) technique,[15–17] and T-matrix techniques,[18–21] but new theories have been developed for the rapid calculation of scattering from

G. Videen (videen@atm.dal.ca) is with the U.S. Army Research Laboratory, 2800 Powder Mill Road, Adelphi, Maryland 20783-1197. W. Sun and Q. Fu are with the Atmospheric Sciences Program, Department of Oceanography, Dalhousie University, Halifax, Nova Scotia B3H 4J1 Canada. D. R. Secker, R. Greenaway, P. H. Kaye, and E. Hirst are with the Science and Technology Research Centre, University of Hertfordshire, Hatfield AL10 9AB UK. D. Bartley is with the National Institute for Occupational Safety and Health, Cincinnati, Ohio 45226.

Received 10 January 2000; revised manuscript received 19 June 2000.

0003-6935/00/275031-09$15.00/0

commonly occurring particle systems such as multiple spheres[22–28] and spheres containing eccentrically located inclusions.[29–32]

In part I[33] we describe methods for routinely acquiring light-scattering data from individual deformed droplets and droplets with inclusions, and examples of the spatial scattering patterns resulting from these particle morphologies are presented. Here we now show how the scatter from these types of particle can be readily calculated (indeed, all the calculations performed here can be made by use of programs that are currently in the public domain[34–36]).

2. Particle Systems

Mie theory predicts the electromagnetic fields scattered by a homogeneous sphere illuminated by a plane wave. When illuminated by a laser beam of sufficiently large spot size, the light-scattering total intensity can be described by concentric rings about the specular peak that are due to the particle symmetry. The spacing of the rings is determined by sphere composition and, most importantly, by size. Here we describe a number of particle systems created by a vibrating orifice-type droplet generator. The advantage of such generators is that millions of nearly identical particle systems can be created periodically and hence studied in great detail. So reproducible are these systems, that it is even possible to adjust the vibrating frequency, and hence the particle size, and accurately measure the scatter as the particles pass through a resonance.[37,38] As described in part I,[33] under certain measurement conditions the droplets can be predictably distorted to become aspherical. We begin by examining the scatter from some of these distorted droplets.

3. Ellipsoids, Stadium Particles, and other Unidentified Flying Objects

When a normally spherical droplet is subject to an accelerating airflow as, for example, is found in the sampling nozzle of aerodynamic particle-sizing instruments, it can be made to distort into one of a range of geometries, the simplest of which is spheroidal. Calculation of the scattering from spheroids is now commonplace. Several methods exist for doing this, but perhaps the most common is the T-matrix approach first developed by Waterman.[18,19] T-matrix techniques have many inherent advantages. Because of their efficient use of vector spherical harmonics, they are rapid and provide an efficient way to calculate scattering properties when a particle system is illuminated at different scattering angles. An excellent review article of this technique has been published by Mishchenko *et al.*[21] who also maintains a website containing the source code to calculate the scattering from spheroids.[35]

Despite the advantages of the T-matrix method, for a number of reasons we performed the calculations in this section using the FDTD algorithm with a perfectly absorbing boundary layer.[15] First, extreme computational precision is necessary when one is calculating the T matrix of particles having large aspect ratios, some of which we wished to analyze. Second, improvements in the FDTD to include a perfectly absorbing boundary layer are accurate to well within a percent at all scattering angles except at minima where the scattering is several orders of magnitude lower than the maxima.[39] Third, FDTD methods no longer have severe size-parameter restrictions.[15] And fourth, the FDTD algorithm was developed in-house, making it especially easy to modify to our needs. In this section we study a number of droplets having different shapes. For comparison, the refractive index n, maximum physical extent D, and aspect ratio are identical for the particles we discuss in this section. In this way we hope to see the effects of the particle shape on the scattering and see what, if any, distinguishing features appear in the scattering patterns which can help in the inversion procedure. In the simulations we present here, the aspect ratio is set to 2, the refractive index $n = 1.4599$ (corresponding to oleic acid at $\lambda = 0.6328$ μm), and the maximum physical extent is $D = 24\lambda/\pi = 4.83$ μm. We present some examples of the theoretical scatter from nonspherical droplets in Fig. 1. The particles in Fig. 1 are axisymmetric about the z axis and are illuminated by a plane wave traveling in the positive $\hat{x}$ direction so that the forward scatter is located at the center of the graphs ($\theta = 90°$, $\phi = 0°$). The y axis of our plots is the polar angle θ, the x axis is the azimuthal angle ϕ, and the gray level shows the logarithm of the total intensity. Because of the droplet symmetry, the scattering intensities are symmetric about $\theta = 90°$ and $\phi = 0°$.

Figure 1(a) shows the scatter from an oblate spheroid illuminated broadside. Because scattering spatial frequencies are typically inversely proportional to particle dimensions, we expect to see the approximately elliptical concentric rings whose major axis is oriented with the particle's minor axis and vice versa. The dark horizontal bands in Fig. 1(a) are not expected. The position of these bands is dependent on the particle size. As the particle size increases, the number of bands increases and their spacing decreases. Elliptical fringes and multiple interference bands are also displayed in experimental scattering measurements; for example, one clear example is given in part I[33] in Fig. 4 for a 16-μm-equivalent sphere and a flow rate of 5.0 l/min. Because the particle is relatively large, a high number of fringes can be seen in this example.

Some of the particle images demonstrated in part I[33] suggest that under certain conditions of droplet size, viscosity, surface tension, and airflow acceleration, droplets tend to flatten out further and become stadium particles. Stadium cylinders recently garnered some notoriety because scattered rays from such systems have chaotic properties.[40,41] Such systems are produced mathematically when an infinite cylinder is sliced in half lengthwise, pulling the two half-cylinders apart and filling in the gap so that the cross section resembles a rectangle capped with two semicircles, or a stadium. For three-dimensional particles, there are multiple ways to create particles

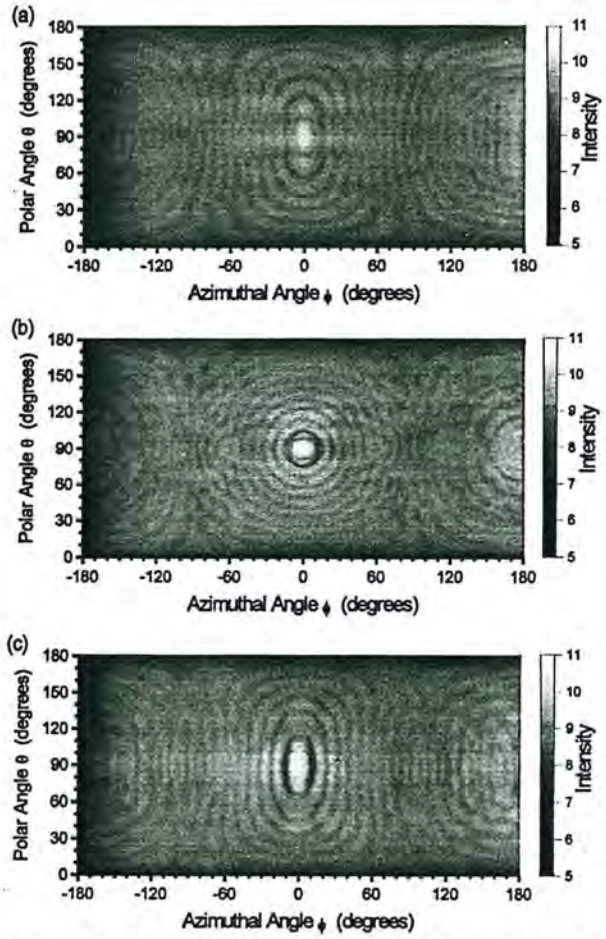

Fig. 1. TAOS calculated from a number of aspherical oleic acid (n = 1.4599) droplets illuminated broadside at λ = 0.6328 μm. The ratio of the largest dimension to the smallest dimension is set equal to 2 for all cases, and the size parameter (in terms of the largest particle extent D) is $x = \pi D/\lambda = 24$. The forward scattering is located at the center of the graphs. The droplet shapes are as follows: (a) an oblate ellipsoid, (b) a stadium sphere resembling a jelly donut, (c) a droplet of the form $r = r_0 + d\,(1 - 3\cos^2\theta)$.

with a stadium cross section: a rod capped with two hemispheres or a finite circular disk having rounded edges (also resembling a jelly donut) both have similar cross sections, so both should display similar chaotic properties. Because stadium rods and disks do not have edges or discontinuities in their spatial derivatives, they are used to simulate finite cylinders and plates in scattering calculations. The scattering from the stadium particle resembling a jelly donut is shown in Fig. 1(b). The scattering from this system is significantly different from that of an ellipsoid. Two distinct sets of fringes are visible. Concentric circular fringes are the result of the spherical caps. Superimposed on this pattern are concentric ovals, elongated in the horizontal direction. The nearly flat edges of the scattering fringes are due to the edge of the disk. Interestingly, none of the experimental patterns shown in part I[33] displayed these characteristics. We present these examples to demonstrate how sensitive the scattering is to particle shape. The particles in Figs. 1(a) and 1(b) have the same dimensions and only vary slightly in shape, but their scattering is significantly different.

We consider one other particle shape in this section, that of a quadrupole toroidal, shown again in part I.[33] This type of distorted droplet, similar in shape to a human erythrocyte (red blood cell) is produced in an accelerating flow field and can be calculated analytically through the Navier–Stokes equation.[42] The droplet is of the form

$$r = r_0 + d(1 - 3\cos^2\theta), \tag{1}$$

where r_0 is the radius of an undistorted droplet and d is the amount of distortion. The droplet is axisymmetric about the z axis. For the droplet to have an aspect ratio of 2, the amount of distortion $d = 0.246r_0$. The scattering from this particle displays a semielliptic ring structure similar to that of the oblate spheroid particle shown in Fig. 1(a), but instead of the multiple bands seen for the spheroid, this particle displays a single high-intensity streak running through the minor axis of the scatter ellipses. Faint, dark bands radiate from the center of the scattering pattern in the form of an x. This scattering pattern bears a strong resemblance to several of the experimental patterns shown in part I (Figs. 4 and 5).[33]

4. Satellites

Depending on the vibrating frequency and droplet size and composition, droplets ejected from the vibrating orifice may break up or come into close proximity with other droplets.[43] In such cases, the resulting scattering system resembles either two spheres of nearly identical size or one large (host) sphere with a much smaller (satellite) sphere in close proximity. It may be impossible to optically isolate the multiple droplets, and the resulting scattered light is the superposition of the scattered light from both particles. Depending on the relative proximity of the droplets, a significant amount of interaction may occur between the two subparticle systems. Many theoretical solutions to the scattering from multiple particle subsystems have been derived[10,22–28] and programmed.[34] To reach a solution is relatively straightforward. The scattered field from every subsystem is considered to be part of the incident field on every other subsystem. One can reach the solution by performing vector translations of these scattered fields from one subsystem coordinate system onto the other subsystem coordinate systems and satisfying the boundary conditions at the interfaces of every subsystem. This process requires knowledge of how to translate vector spherical harmonics from one coordinate system to another and the T matrix for each subsystem. For spherical particles many symmetries exist in the T matrix; and when only two spherical droplets are considered, additional symmetries in the translation coefficients make the calculations rapid. For the calculations in this section we use the

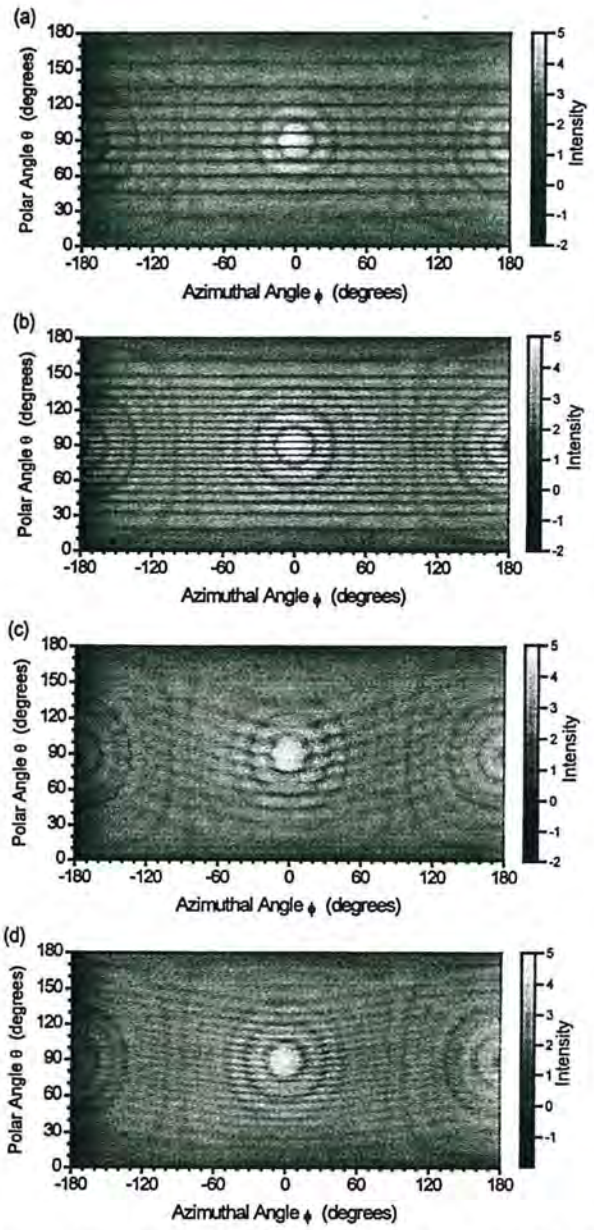

Fig. 2. TAOS calculated from a pair of spherical oleic acid (n = 1.4599) droplets illuminated at λ = 0.6328 μm. The forward scattering is located at the center of the graph and the radii and droplet center separation distances are (a) $r_1 = r_2 = 2\lambda$, $d = 5\lambda$; (b) $r_1 = r_2 = 2\lambda$, $d = 10\lambda$; (c) $r_1 = 2\lambda$, $r_2 = \lambda/2$, $d = 5\lambda$; (d) $r_1 = 2\lambda$, $r_2 = \lambda/2$, $d = 10\lambda$.

program developed by Videen *et al.*[27] that is available at the website maintained by Wriedt.[34]

In our studies we examine two spheres approximating two oleic acid droplets (n = 1.4599) illuminated at λ = 0.6328 μm. Droplets exit the vibrating orifice along the negative z axis. Because of spatial constraints of the experimental system, they are illuminated by a laser beam whose wave vector is perpendicular to this droplet flow. The incident wave vector is in the $\hat{x}$ direction, so the droplets are illuminated broadside. We vary the droplet radii r_1 and r_2 and separation distance d between the droplets and examine the dependence of scattering features on these parameters. Figure 2(a) shows the scattering from a pair of equal-radii $r_1 = r_2 = 2\lambda$ spheres whose centers are separated by a distance $d = 5\lambda$. The forward-scatter ($\theta = 90°$, $\phi = 0°$) maximum is surrounded by concentric rings of minima and maxima, similar to what we would expect from a single Mie sphere. Because of the droplet symmetry, the scattering intensities are symmetric about $\theta = 90°$ and $\phi = 0°$. The major effect of the scattering from two spheres is the interference that is visible in Fig. 2(a) as maxima and minima at constant θ. The minima are most apparent. These minima are due to the interference of the rays scattered by the identical droplets, and their positions depend primarily on the separation distance d. If there is no interaction between the spheres, the scattering from the spheres would be identical except for a phase term. The intensity of the minima would be zero, and the minima positions would depend solely on the separation distance d. Because there is some interaction between the spheres, the minima are not zero. As d increases, the spacing between the minima decreases, as demonstrated in Fig. 2(b), which shows the scattering from the pair of spheres shown in Fig. 2(a), but separated by $d = 10\lambda$. Because the interaction decreases with distance, the intensity values of the minima are lower in Fig. 2(b) than in Fig. 2(a). Young's two-slit experiment is a similar system, and we would expect similar results. Ignoring interaction, we would expect maxima to be located at

$$m\lambda = d \cos\theta, \tag{2}$$

where m is an integer, and we note that θ is the polar angle and not the angle measured from specular. Equation (2) holds quite well even for spheres in close proximity such as those of Fig. 2(a).

When the spheres are not identical, the interference structure becomes distorted. Figure 2(c) shows the light-scattering intensities for a pair of spheres separated by the same spacing as the case of Fig. 2(a), but with the top sphere four times smaller than the bottom sphere ($r_1 = 4r_2 = 2\lambda$). In this projection the minima are no longer lines of constant θ. The contours of the minima now curve toward the larger particle as the magnitude of ϕ increases. As the separation distance between the particles increases [shown in Fig. 2(d)], the spacing between the minima decreases and the slopes of the minima also decrease. The positions of the nodes and antinodes can be approximated quite simply with a ray-tracing model. Figure 3 shows a diagram of the two spheres and the rays that produce the interferogram. In this model we assume that only the rays reflecting off the outer surfaces of the spheres contribute to the interference. Ray 1 strikes the surface of sphere 1 of radius r_1 placed a distance d below sphere 2 of radius r_2, which is struck by ray 2. Both rays are scattered to the

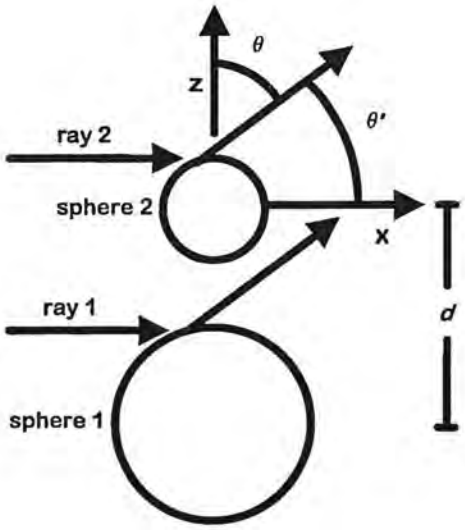

Fig. 3. Configuration of the model used to estimate the shape of the scattering maxima produced by two spheres. Sphere 1 of radius r_1 is located a distance d below sphere 2 of radius r_2. Each sphere is struck by a ray that is reflected off the surface to a detector placed in the far field at (θ, ϕ). The constructive interference of these two rays can be used to predict the locations of interference maxima.

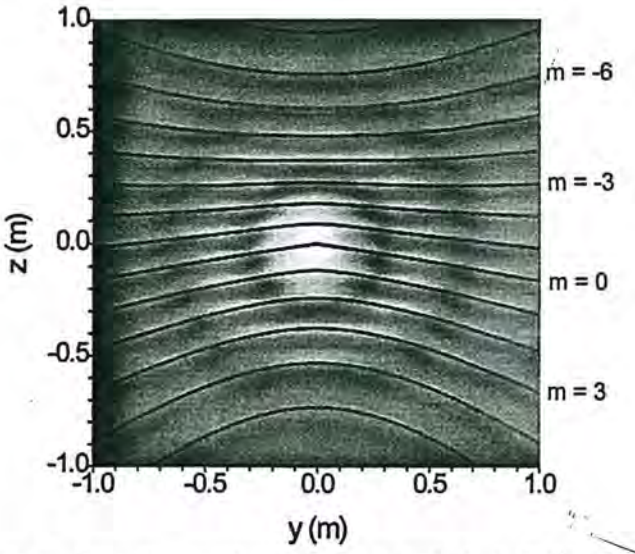

Fig. 4. Scattering interferogram of a pair of spherical oleic acid ($n = 1.4599$) droplets illuminated at $\lambda = 0.6328$ μm. The radii of the droplets are $r_1 = 2\lambda$, $r_2 = \lambda/2$, and the droplet center separation distance $d = 10\lambda$. Superimposed are the shapes of the scattering maxima predicted with Eq. (4).

detector placed in the far field at (θ, ϕ). The phase difference between these two rays can be written as

$$\Phi = kd \cos\theta + 2k(r_1 - r_2)\sin\frac{\theta'}{2}, \qquad (3)$$

where k is the wave number of the incident light, θ is the scattering angle measured from the z axis connecting the centers of the spheres, and θ' is the scattering angle measured from the specular direction (x axis). For the rays to interfere constructively and a maximum to appear in the scattering, the path difference between the rays must be an integer number of wavelengths. If we project the pattern onto a screen, it is convenient to express the condition for a maximum [Eq. (3)] as

$$m\lambda = dz/\sqrt{x^2 + y^2 + z^2} + (r_2 - r_1)\sqrt{2}(1 - x/\sqrt{x^2 + y^2 + z^2})^{1/2}, \qquad (4)$$

where m is an integer. Note that if the spheres are the same size ($r_1 = r_2$), the interference is due solely to the separation distance between the spheres and the maxima trace lines of constant θ [from Eq. (3)], which are shown in Figs. 2(a) and 2(b). On a screen placed parallel to the y–z plane, Eq. (4) is simplified and these maxima are hyperbolae.

When the spheres are not the same size, the interferogram is more complicated; however, the ray-tracing solution does an adequate job of reproducing the maxima. Figure 4 shows the interferogram of Fig. 2(d) projected on a screen placed at $x = 1$ m from the centers of the spheres. Superimposed on the pattern are lines predicting the position of the maxima by use of Eq. (4), which assumes that forward-scattered rays from each individual particle are in phase. In general, this is not the case. The result is that the predicted maxima positions are displaced. Although the predicted positions of the maxima are different from the actual positions, the contours of the maxima and the spacing between them is accurate. This is remarkable considering that we use a ray-tracing model and include only singly reflected rays when the size of the spheres are of the order of the wavelength, and refraction, interaction, and diffraction are completely ignored in the model. Part of the reason for the good agreement is that the change in the phase of the individual scattering amplitudes resulting from this simple model as a function of scattering angle qualitatively agrees with reality.

5. Inclusions

When the composition of the liquid placed in the reservoir of the vibrating orifice droplet generator is inhomogeneous, the droplets produced by the generator may also be inhomogeneous. One type of system commonly studied is that of a liquid host containing polystyrene spheres.[37,44–52] The resonance structure and lasing properties of the host droplet have a strong dependence on the size and quantity of spherical inclusions. Such systems are easily produced, but to quantify the position and placement of the inclusions is difficult. As demonstrated in part I,[33] when oleic acid droplets are created in a humid environment, it is hypothesized that water condenses onto the droplet creating an immiscible oleic acid and water droplet. Because of the symmetry, the location of the water inclusion within the oleic acid host is centered on the z axis. Such a system is of interest from a modeling point of view

because it contains one relatively large inclusion whose position is at least restricted to a single axis.

Many theoretical solutions to the scattering from spherical hosts containing subsystems have been derived[29–32] and programmed.[34,53] The solution is relatively straightforward. The scattered field from every subsystem within the host is considered to be part of the incident field on every other subsystem and as part of the internal fields of the host. The solution can be reached when one performs vector translations of these scattered fields from each subsystem coordinate system onto the host sphere coordinate system and satisfies the boundary conditions at all the interfaces. Like the two-sphere system, this process requires knowledge of how to translate vector spherical harmonics from one coordinate system to another and the T matrix for every system. For spherical inclusions many symmetries exist in the T matrix; and when only a single spherical inclusion is considered, additional symmetries in the translation coefficients make the calculations rapid. For the calculations in this section we use the program developed by Videen *et al.*[32] that is available at the website maintained by Wriedt.[34]

In our studies we examine a spherical host oleic acid droplet ($n = 1.4599$) containing a water inclusion ($n = 1.33$) illuminated at $\lambda = 0.6328$ μm. Droplets exit the vibrating orifice along the negative z axis. Because of spatial constraints of the experimental system, they are illuminated by a laser beam whose wave vector is perpendicular to this droplet flow (the incident wave vector is in the $\hat{x}$ direction). Because of the symmetry, we assume the water inclusion to be centered on this line of flow, the z axis.

The most dramatic effect is the dependence of spatial scattering on the position of the inclusion. We demonstrate this dependence in Fig. 5, which shows the TAOS calculated from a spherical $r_1 = 5\lambda$ oleic acid host droplet containing a spherical $r_2 = 2.5\lambda$ water inclusion illuminated at $\lambda = 0.6328$ μm. Data from four different inclusion positions are shown. Parameter d is the distance from the center of the host droplet to the center of the inclusion. Figure 5(a) shows the scattering when the spheres are concentric, $d = 0$. In this case the bright central maximum ($\theta = 90°$, $\phi = 0°$) is surrounded by concentric minima and maxima. Because of the symmetry, the scattering from the concentric sphere system is similar to that of a homogeneous sphere. As the inclusion is moved from the center of the host particle, the symmetry is broken and additional structure is apparent in the spatial scattering. Figure 5(b) shows the scattering when the inclusion is displaced one wavelength in the $\hat{z}$ direction from the host center. Although the symmetric fringe pattern that can be seen in Fig. 5(a) remains the dominant feature, additional structure is now present. A few degrees above the central maximum (on the side opposite the inclusion), the pattern is noticeably brighter than in Fig. 5(a), whereas a few degrees below the central maximum the pattern is noticeably darker. If we look further from the central maximum (approximately 30°) this is reversed, and it is darker above the central maximum and lighter below. As the inclusion is brought closer to the edge of the host [Fig. 5(c)], a secondary ring structure becomes apparent in the scattering, centered approximately 30° above the specular peak (in the direction opposite the inclusion). In addition, two dark bands radiate outward from the specular peak forming a vee in this projection. When the inclusion is brought to the edge of the host [Fig. 5(d)], the secondary structure changes position only slightly, but the contrast has also increased slightly. In addition, the minima nearest the specular are distorted and are distended on the

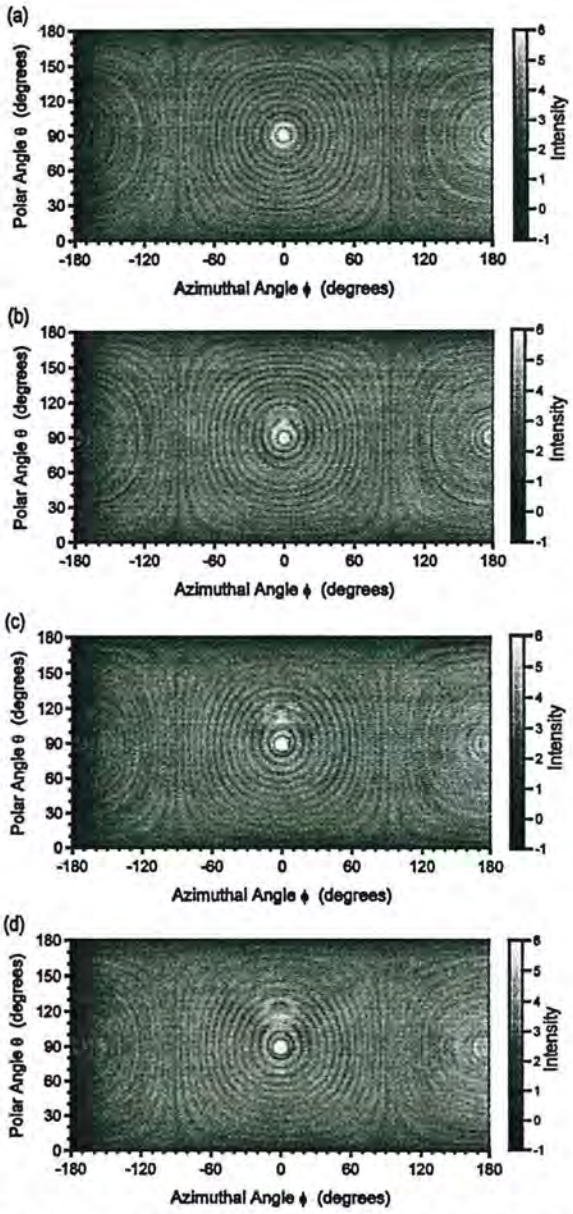

Fig. 5. TAOS calculated from a spherical $r_1 = 5\lambda$ oleic acid ($n = 1.4599$) host droplet containing a spherical $r_2 = 2.5\lambda$ water ($n = 1.33$) inclusion illuminated at $\lambda = 0.6328$ μm. The distance from the inclusion center to host center is (a) $d = 0\lambda$, (b) $d = 1.0\lambda$, (c) $d = 2.0\lambda$, and (d) $d = 2.4\lambda$.

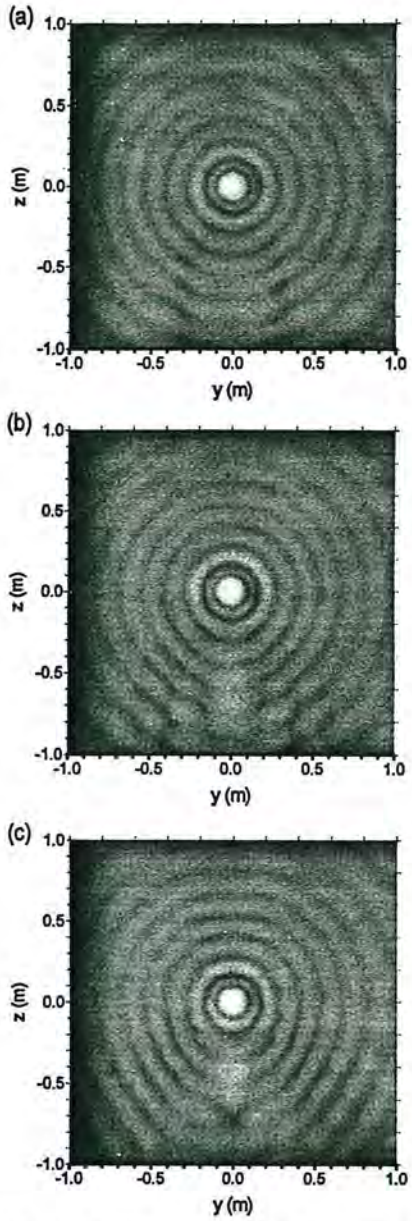

Fig. 6. TAOS calculated from a spherical $r_1 = 6\lambda$ oleic acid ($n = 1.4599$) host droplet containing a spherical water ($n = 1.33$) inclusion whose center is located a distance $d = 3.0\lambda$ from the host center. The inclusion radius is (a) $r_2 = 1\lambda$, (b) $r_2 = 2\lambda$, and (c) $r_2 = 2.99\lambda$.

side of the inclusion. The dominant features in Fig. 5 are present in the experimental scattering measurements of the oleic acid host droplets containing water inclusions made by the authors and shown in part I (Figs. 8 and 9).[33]

Figure 6 shows the scattering from three $r_1 = 6.0\lambda$ oleic acid host droplets containing different size spherical water inclusions placed at the same position within the host. The scattering is projected onto a plane screen placed 1 m from the particle system. Note that the primary ring structure in this projection is now circular and that the secondary interference is below the specular (still opposite the inclusion). Figure 6(a) shows the scattering when the inclusion radius is $r_2 = 1.0\lambda$. Only one secondary ring is obvious for this system. As the inclusion size increases to $r_2 = 2.0\lambda$ [Fig. 6(b)], the frequency of the secondary rings increases and so does the contrast. When the inclusion size is further increased [Fig. 6(c)], these features are enhanced. In this series of scatter plots, it is apparent that the secondary ring structure is the result of host internal fields being scattered by the inclusion. Upon exiting the host droplet, these fields are refracted to the side opposite the specular peak. The frequency of this secondary ring structure is related directly to the size of the inclusion. In previous experimental research,[44] cross-polarized images of host droplets containing inclusions have been described as a "ring of fireflies" which flash on and off when the inclusions enter and leave the outer (high-intensity internal field) region of the host. This observation is consistent with our simulations that show the secondary ring structure to be more visible when the inclusions are near the outer edge of the host.

6. Conclusion

In this paper we calculated the spatial scattering from droplets having different morphologies. The theoretical scattering patterns produced here can all be replicated with programs available in the public domain and, as shown in part I, can be routinely and reproducibly generated experimentally with a vibrating orifice droplet generator and an aerodynamic focusing nozzle. Many of the features present in the light-scattering data not only identify the fundamental geometry of the particle, but can be used to quantify particle characteristics such as the degree of deformation of droplets from their normal spherical form or the presence of inclusions within droplets. The former is of importance when aerodynamic particle-sizing instruments are used to assess droplet behavior; the latter has importance in the field of bioaerosol detection. In the case of bisphere scattering, the interferogram produced can be reproduced quite accurately with the ray-tracing model we presented in this paper. After experimentally capturing an interferogram, it would be relatively trivial for one to perform a curve fit to the secondary maxima to identify the particle sizes and relative positions.

This research was carried out with funding from the UK Engineering and Physical Sciences Research Council and with support from TSI Inc., St. Paul, Minn., and U.S. Department of Energy, Atmospheric Radiation Measurement Program grant DE-FG02-97ER62363.

References and Notes

1. W. D. Griffiths, P. J. Iles, and N. P. Vaughan, "The behaviour of liquid droplets in an APS 3300," J. Aerosol Sci. **17,** 427–431 (1986).
2. R. G. Pinnick, S. C. Hill, P. Nachman, G. Videen, G. Chen, and R. K. Chang, "Aerosol fluorescence spectrum analyzer for measurement of single micron-sized airborne biological particles," Aerosol Sci. Technol. **28,** 95–104 (1998).

3. J. Barton, E. Hirst, P. Kaye, S. Saunders, and D. Clark, "Airborne particle characterization by spatial scattering and fluorescence," in *Air Monitoring and Detection of Chemical and Biological Agents II*, J. Leonelli and M. L. Althouse, eds., Proc. SPIE **3855,** 92–100 (1999).
4. A. Ashkin and J. M. Dziedzic, "Observation of light scattering from nonspherical particles using optical levitation," Appl. Opt. **19,** 660–668 (1980).
5. S. Holler, Y.-L. Pan, R. K. Chang, J. R. Bottiger, S. C. Hill, and D. B. Hillis, "Two-dimensional angular optical scattering for the characterization of airborne microparticles," Opt. Lett. **23,** 1489–1491 (1998).
6. S. Holler, M. Surbek, R. K. Chang, and Y.-L. Pan, "Two-dimensional angular optical scattering patterns as droplets evolve into clusters," Opt. Lett. **24,** 1185–1187 (1999).
7. M. D. Barnes, C.-Y. Kung, N. Lermer, K. Fukui, B. G. Sumpter, D. W. Noid, and J. U. Otaigbe, "Homogeneous polymer blend microparticles with a tunable refractive index," Opt. Lett. **24,** 121–123 (1999).
8. B. Sachweh, H. Barthel, R. Polke, H. Umhauer, and H. Büttner, "Particle shape and structure analysis from the spatial intensity pattern of scattered light using different measuring devices," J. Aerosol Sci. **30,** 1257–1270 (1999).
9. P. H. Kaye, K. Alexander-Buckley, E. Hirst, and S. Saunders, "A real-time monitoring system for airborne particle shape and size analysis," J. Geophys. Res. D **101,** 19215–19221 (1996).
10. E. Hirst and P. H. Kaye, "Experimental and theoretical light scattering profiles from spherical and non-spherical particles," J. Geophys. Res. D **101,** 19231–19235 (1996).
11. P. H. Kaye, "Spatial light scattering as a means of characterising and classifying non-spherical particles," Meas. Sci. Technol. **9,** 141–149 (1998).
12. B. T. Draine, "The discrete dipole approximation for light scattering by irregular targets," in *Light Scattering by Nonspherical Particles*, M. I. Mishchenko, J. W. Hovenier, and L. D. Travis, eds. (Academic, New York, 1999), pp. 131–145.
13. B. T. Draine and P. J. Flatau, "Discrete-dipole approximation for scattering calculations," J. Opt. Soc. Am. A **11,** 1491–1499 (1994).
14. A. Hoekstra, J. Rahola, and P. Sloot, "Accuracy of internal fields in volume integral equation simulations of light scattering," Appl. Opt. **37,** 8482–8497 (1998).
15. W. Sun, Q. Fu, and Z. Chen, "Finite-difference time-domain solution of light scattering by dielectric particles with a perfectly matched layer absorbing boundary condition," Appl. Opt. **38,** 3141–3151 (1999).
16. P. Yang and K. N. Liou, "Finite difference time domain method for light scattering by nonspherical and inhomogeneous particles," in *Light Scattering by Nonspherical Particles*, M. I. Mishchenko, J. W. Hovenier, and L. D. Travis, eds. (Academic, New York, 1999), pp. 173–221.
17. K. S. Yee, "Numerical solution of initial boundary value problems involving Maxwell's equation in isotripic media," IEEE Trans. Antennas Propag. **AP-14,** 302–307 (1966).
18. P. C. Waterman, "Matrix formulation of electromagnetic scattering," Proc. IEEE **53,** 805–812 (1965).
19. P. C. Waterman, "Symmetry, unitarity, and geometry in electromagnetic scattering," Phys. Rev. D **3,** 825–812 (1971).
20. M. I. Mishchenko, "*T*-matrix method and its applications," in *Light Scattering by Nonspherical Particles*, M. I. Mishchenko, J. W. Hovenier, and L. D. Travis, eds. (Academic, New York, 1999), pp. 147–172.
21. M. I. Mishchenko, L. D. Travis, and D. W. Mackowski, "*T*-matrix computations of light scattering by nonspherical particles: a review," J. Quant. Spectrosc. Radiat. Transfer **55,** 535–575 (1996).
22. J. H. Bruning and Y. T. Lo, "Multiple scattering of EM waves by spheres parts I&II," IEEE Trans. Antennas Propag. **AP-19,** 378–400 (1971).
23. F. Borghese, P. Denti, R. Saija, G. Toscano, and O. I. Sindoni, "Multiple electromagnetic scattering from a cluster of spheres. I. Theory," Aerosol Sci. Technol. **3,** 227–235 (1984).
24. D. W. Mackowski, "Calculation of total cross sections of multiple-sphere clusters," J. Opt. Soc. Am. A **11,** 2851–2861 (1994).
25. K. A. Fuller, "Scattering and absorption cross sections of compounded spheres. I. Theory for external aggregation," J. Opt. Soc. Am. A **11,** 3251–3260 (1994).
26. K. A. Fuller, "Scattering and absorption cross sections of compounded spheres. II. Calculations for external aggregation," J. Opt. Soc. Am. A **12,** 881–892 (1995).
27. G. Videen, D. Ngo, and M. B. Hart, "Light scattering from a pair of conducting, osculating spheres," Opt. Commun. **125,** 275–287 (1996).
28. K. A. Fuller and D. W. Mackowski, "Electromagnetic scattering by compounded spherical particles," in *Light Scattering by Nonspherical Particles*, M. I. Mishchenko, J. W. Hovenier, and L. D. Travis, eds. (Academic, New York, 1999), pp. 225–272.
29. J. G. Fikioris and N. K. Uzunoglu, "Scattering from an eccentrically stratified dielectric sphere," J. Opt. Soc. Am. **69,** 1359–1366 (1979).
30. F. Borghese, P. Denti, and R. Saija, "Optical properties of spheres containing a spherical eccentric inclusion," J. Opt. Soc. Am. A **9,** 1327–1335 (1992).
31. K. A. Fuller, "Scattering and absorption cross sections of compounded spheres. III. Spheres containing arbitrarily located spherical inhomogeneities," J. Opt. Soc. Am. A **12,** 893–904 (1995).
32. G. Videen, D. Ngo, P. Chýlek, and R. G. Pinnick, "Light scattering from a sphere with an irregular inclusion," J. Opt. Soc. Am. A **12,** 922–928 (1995).
33. D. R. Secker, P. H. Kaye, R. S. Greenaway, E. Hirst, D. L. Bartley, and G. Videen, "Light scattering from deformed droplets and droplets with inclusions. I. Experimental results," Appl. Opt. **39,** 5023–5030 (2000).
34. Website maintained by T. Wriedt: http://imperator.cip-iw1.uni-bremen.de/fg01/codes2.html.
35. Website maintained by M. I. Mishchenko: http://www.giss.nasa.gov/~crmim/.
36. Website maintained by P. J. Flatau: http://atol.ucsd.edu/~pflatau/.
37. D. Ngo and R. G. Pinnick, "Suppression of scattering resonances in inhomogeneous microdroplets," J. Opt. Soc. Am. A **11,** 1352–1359 (1994).
38. A. Biswas, H. Latifi, R. L. Armstrong, and R. G. Pinnick, "Time-resolved spectroscopy of laser emission from dye-doped droplet," Opt. Lett. **14,** 214–216 (1989).
39. G. Videen, W. Sun, and Q. Fu, "Light scattering from irregular tetrahedral aggregates," Opt. Commun. **156,** 5–9 (1998).
40. J. H. Jensen, "Chaotic scattering of light by a dielectric cylinder," J. Opt. Soc. Am. A **10,** 1204–1208 (1993).
41. J. U. Nöckel and A. D. Stone, "Ray and wave chaos in asymmetric resonant optical cavities," Nature (London) **385,** 45–47 (1997).
42. D. L. Bartley, A. B. Martinez, P. A. Baron, D. R. Secker, and E. Hirst, "Droplet distortion in accelerating flow," J. Aerosol Sci. (to be published).
43. H.-J. Moon, G.-H. Kim, Y.-S. Lim, C.-S. Go, J.-H. Lee, and J.-S. Chang, "Lasing images from two merging ink-doped liquid droplets," Opt. Lett. **21,** 913–915 (1996).
44. B. V. Bronk, M. J. Smith, and S. Arnold, "Photon-correlation spectroscopy for small spherical inclusions in a micrometer-sized electrodynamically levitated droplet," Opt. Lett. **18,** 93–95 (1993).

45. J. Gu, T. E. Ruekgauer, J.-G. Xie, and R. L. Armstrong, "Effect of particulate seeding on microdroplet angular scattering," Opt. Lett. **18,** 1293–1295 (1993).
46. J.-G. Xie, T. E. Ruekgauer, R. L. Armstrong, and R. G. Pinnick, "Suppression of stimulated Raman scattering from microdroplets by seeding with nanometer-sized latex particles," Opt. Lett. **18,** 340–342 (1993).
47. H.-B. Lin, A. L. Huston, J. D. Eversole, A. J. Campillo, and P. Chýlek, "Internal scattering effects on microdroplet resonant emission structure," Opt. Lett. **17,** 970–972 (1992).
48. R. L. Armstrong, J.-G. Xie, T. E. Ruekgauer, J. Gu, and R. G. Pinnick, "Effects of submicrometer-sized particles on microdroplet lasing," Opt. Lett. **18,** 119–121 (1993).
49. T. Kaiser, G. Roll, and G. Schweiger, "Enhancement of the Raman spectrum of optically levitated microspheres by seeded nanoparticles," J. Opt. Soc. Am. B **12,** 281–286 (1995).
50. G. Videen, P. Pellegrino, D. Ngo, J. S. Videen, and R. G. Pinnick, "Light-scattering intensity fluctuations in microdroplets containing inclusions," Appl. Opt. **36,** 6115–6118 (1997).
51. G. Videen, P. Pellegrino, D. Ngo, P. Nachman, and R. G. Pinnick, "Qualitative light-scattering angular correlations of conglomerate particles," Appl. Opt. **36,** 3532–3537 (1997).
52. P. Pellegrino, G. Videen, and R. G. Pinnick, "Quantitative light-scattering angular correlations of conglomerate particles," Appl. Opt. **36,** 7672–7677 (1997).
53. D. Ngo, G. Videen, and P. Chýlek, "A FORTRAN code for the scattering of EM waves by a sphere with a nonconcentric spherical inclusion," Comput. Phys. Commun. **1077,** 94–112 (1996).